



Article

The High-Energy Milling Preparation and Spectroscopic Characterization of Rare-Earth Ions Doped BaY₂F₈ Nanoparticles

Aleksander V. Koshelev ^{1,*}, Natalia A. Arkharova ¹, Kirill V. Khaydukov ¹, Mir Saeed Seyed Dorraji ² , Denis N. Karimov ^{1,*}  and Vera V. Klechkovskaya ¹

¹ Federal Scientific Research Center «Crystallography and Photonics», Russian Academy of Sciences, Leninsky Prospekt 59, 119333 Moscow, Russia; natalya.arkharova@yandex.ru (N.A.A.); khaydukov_11@mail.ru (K.V.K.); klechvv@crys.ras.ru (V.V.K.)

² Applied Chemistry Research Laboratory, Department of Chemistry, Faculty of Science, University of Zanjan, Zanjan 45371-38791, Iran; dorraji@znu.ac.ir

* Correspondence: avkoshelev03@gmail.com (A.V.K.); dnkarimov@gmail.com (D.N.K.); Tel.: +7-977-577-28-46 (A.V.K.); +7-903-778-74-89 (D.N.K.)

Abstract: BaY₂F₈ nanoparticles (NPs), doped with Yb³⁺ and Er³⁺ ions, were successfully produced by high-energy ball-milling. High-quality monoclinic single crystals (sp. gr. *C*₂/*m*, *a* = 0.6969(3), *b* = 1.0502(1), *c* = 0.4254(1) nm, β = 99.676°) grown from the melt by the Bridgman technique were used as raw materials. The prepared nanocrystals were comprehensively studied by X-ray diffraction analysis, transmission electron microscopy, and optical spectroscopy. The fabrication possibility of single-phase irregular shaped Ba(Y_{0.964}Yb_{0.030}Er_{0.006})₂F₈ NPs in the size range of 20–100 nm with a milling duration of 10 h at 600 rpm is demonstrated. Ba(Y_{0.964}Yb_{0.030}Er_{0.006})₂F₈ NPs show intense luminescence by both up- (λ = 540 and 650 nm) and down-conversion (λ = 1540 nm) mechanisms upon IR excitation (λ = 980 nm). A qualitative comparison of the spectroscopic characteristics of the produced Ba(Y_{0.964}Yb_{0.030}Er_{0.006})₂F₈ NPs with the initial bulk crystal and the widely used up-conversion β-Na_{1.5}(Y_{1.17}Yb_{0.3}Er_{0.03})F₆ NPs is presented. Experimental data offer great opportunities of the Ba(Y_{0.964}Yb_{0.030}Er_{0.006})₂F₈ NPs applications in nanophotonics and biotechnology. High-energy ball-milling has potential as a versatile method for the scalable production of fluoride nanoparticles.

Keywords: inorganic fluoride; rare-earth elements; bulk crystal; nanoparticle; BaY₂F₈; luminescence



Citation: Koshelev, A.V.; Arkharova, N.A.; Khaydukov, K.V.; Seyed Dorraji, M.S.; Karimov, D.N.; Klechkovskaya, V.V. The High-Energy Milling Preparation and Spectroscopic Characterization of Rare-Earth Ions Doped BaY₂F₈ Nanoparticles. *Crystals* **2022**, *12*, 599. <https://doi.org/10.3390/cryst12050599>

Academic Editors: Anatoliy V. Glushchenko and Alexey Voloshin

Received: 29 March 2022

Accepted: 22 April 2022

Published: 24 April 2022

Publisher's Note: MDPI stays neutral with regard to jurisdictional claims in published maps and institutional affiliations.



Copyright: © 2022 by the authors. Licensee MDPI, Basel, Switzerland. This article is an open access article distributed under the terms and conditions of the Creative Commons Attribution (CC BY) license (<https://creativecommons.org/licenses/by/4.0/>).

1. Introduction

Photoluminescent (PL) nanomaterials doped with rare-earth elements (REE) have become an important basis for various photonic applications: biomedicine, photocatalysis, nanosensors, anti-counterfeiting, etc. [1–7]. Among the variety of the inorganic materials, the development of REE-doped fluoride NPs attracts special attention due to high chemical and thermal stability, low phonon frequencies, wide optical transparency, high isomorphous capacity, and a large selection of different dopants [7,8]. These unique features provide the ability to generate luminescence in a wide spectral range. Currently, approaches for the chemical synthesis (hydro-, solvothermal methods, coprecipitation, etc.) of fluoride NPs, based on different REE-doped crystal hosts, such as MF₂ (*M* = Ca, Sr, Ba), LiRF₄, NaRF₄, BaRF₅, KR₃F₁₀, and RF₃, (*R* = Y, La–Lu) have been successfully developed [9–16], and hexagonal β-NaRF₄ NPs demonstrate excellent up-conversion emission upon IR excitation [8,17]. However, the active development of new types of highly efficient nanophosphors continues at present. The preparation of new prospective fluoride hosts is limited by the technological capabilities of existing chemical techniques, which explains the active interest in the search for alternative physical “top-down” approaches, such as laser ablation [18,19] or mechanical milling (nanodispersion) of initial bulk materials [20,21].

Among fluoride PL nanocrystals, host compounds formed in the BaF₂–YF₃ binary system attract significant interest, and their potential for photonic and biological applications

is being actively studied. There are three crystal matrices in the $\text{BaF}_2\text{-YF}_3$ system [22]: a fluorite solid solution $\text{Ba}_{1-x}\text{Y}_x\text{F}_{2+x}$ ($x < 0.36$); a trigonal phase (sp. gr. $R\bar{3}$) with nominal composition $\text{Ba}_{4\pm x}\text{Y}_{3\pm x}\text{F}_{17}$, existing in the middle concentration range [23]; and a monoclinic BaY_2F_8 phase (sp. gr. C_2/m) [24]. Effective luminescence generation in BaYF_5 and BaY_2F_8 bulk crystal hosts doped with various REE combinations was first demonstrated in 1969 [25]. REE-doped BaY_2F_8 single crystals have been studied as active laser media in a wide spectral range both up- and down-conversion excitation schemes [26–30]. These crystals are considered as promising scintillation materials in the vacuum UV and visible regions due to high ionizing radiation resistance [31–33].

The modern trend in the search for new efficient PL inorganic materials is focused on the nanoscale. Wet chemical methods for the synthesis of BaYF_5 NPs with different crystal structures (cubic [14,34,35] or tetragonal [36–38]) were developed in detail, and the applications of these nanocrystals in bioimaging, optical thermometry, and white light emitting devices have been described. However, the stoichiometric composition of these particles needs to be specified due to the nonequilibrium state of the system during the synthesis. These BaYF_5 compounds are probably the metastable fluorite-type solid solutions [39,40]. At the same time, the synthesis strategies for $\text{Ba}_4\text{Y}_3\text{F}_{17}$ and BaY_2F_8 NPs are quite limited, what is associated with the significant technological complexity of preparing single-phase nanosized particles via chemical synthesis [41,42].

Monodisperse “nanobelts” $\text{BaY}_2\text{F}_8\text{:Yb}^{3+}/\text{Er}^{3+}$ with dimensions of $1000 \times 75 \text{ nm}^2$ were synthesized by the liquid–solid solution strategy [43]. $\text{BaY}_2\text{F}_8\text{:Yb}^{3+}/\text{Ho}^{3+}$ compounds were produced by solid-phase fluorination of the corresponding electrospun oxide compositions such as nanofiber [44] or submicrosized particles via co-precipitation in aqueous nitrate solutions [45]. Therefore, the development of a facile production method for BaY_2F_8 NPs is extremely essential.

In this regard, a promising approach for the BaY_2F_8 NPs fabrication is nanonization of raw single-phase bulk crystals via high-energy milling. The advantages of this method are technological simplicity, low cost, scalability, and ecological safety. However, this method is not widely used due to the possibility of pollution with milling set materials and the high polydispersity of the resulting product, which requires additional sedimentation procedures to isolate the nanofraction from larger particles. This technique was previously applied to prepare BaY_2F_8 NPs, doped with Pr^{3+} and $\text{Yb}^{3+}/\text{Tm}^{3+}$ ions [46,47], but the milling procedure is not described in detail. Utilization of such a “top-down” approach to produce new types of REE doped NPs and a comprehensive characterization of their luminescent properties is desirable to extend of photonics and biotechnology possibilities.

In this study, bulk BaY_2F_8 single crystals doped with Yb^{3+} , Er^{3+} ions were grown from the melt by the Bridgman technique, and single-phase NPs were prepared via high-energy milling of these compounds. The size, morphology, and composition of fabricated nanocrystals were characterized by X-ray diffraction (XRD) analysis, transmission electron microscopy (TEM), and optical and fluorescent spectroscopy in a wide wavelength range. Structural and spectroscopic features of $\text{Ba}(\text{Y}_{0.964}\text{Yb}_{0.030}\text{Er}_{0.006})_2\text{F}_8$ NPs were compared with ones for bulk materials and commonly used up-conversion $\beta\text{-Na}_{1.5}(\text{Y}_{1.17}\text{Yb}_{0.3}\text{Er}_{0.03})\text{F}_6$ nanocrystals, prepared by solvothermal method.

2. Materials and Methods

2.1. Crystal Growth Process

$\text{Ba}(\text{Y}_{0.964}\text{Yb}_{0.030}\text{Er}_{0.006})_2\text{F}_8$ single crystals were successfully grown by the Bridgman technique in a double-zone resistive setup in a fluorinating atmosphere. The graphite heating unit and crucible were utilized in the growth process. Anhydrous BaF_2 (99.98%, Angarsk Electrolysis Chemical Plant Ltd., Angarsk, Russia), YF_3 , YbF_3 , and ErF_3 (99.99%, Lanhit Ltd., Moscow, Russia) powders were used as initial reagents. The powders were preliminarily annealed in vacuum at 500 K and melted in a fluorinating atmosphere for purification from oxygen impurities. Preliminary evacuation was carried out to the level of $5 \times 10^{-3} \text{ Pa}$. A high-purity $\text{He} + \text{CF}_4$ mixture was used to create a fluorinating

growth atmosphere. The temperature gradient in the growth zone was 80 K/cm. W-Re thermocouples were used for continuous temperature control. The crucible pulling rate was about 3.5 mm/h. After growth, the crystals were cooled down to room temperature (RT) at a rate of 50 K/h. The losses of the substance due to evaporation during the crystallization process were less than 0.5 wt. %.

2.2. Optical Characterization

Transmission spectra of the crystals were recorded at RT using a Varian Cary 5000 spectrophotometer (Agilent Technologies, Santa Clara, CA, USA) in the spectral region $\lambda = 190\text{--}2000$ nm.

2.3. Nanodispersion of Bulk Crystals

High-energy milling of the grown crystals in the Retsch PM-200 planetary ball mill (Idar-Oberstein, Germany) was carried out for the fabrication of $\text{Ba}(\text{Y}_{0.964}\text{Yb}_{0.030}\text{Er}_{0.006})_2\text{F}_8$ NPs. Crystal pieces with volume of about 0.1 cm^3 were preliminarily pestled in an agate mortar and placed in stainless steel beakers filled with 10 milling balls with a diameter of 10 mm. Trioctylphosphine oxide was used as a surface stabilizer to prevent NPs agglomeration. The crystals were milled in cycles of 5×5 min at 600 rpm for 10 h. Separation of the nanosized fraction was performed through centrifugation at 6000 rpm for 15 min.

2.4. Synthesis of Reference $\beta\text{-Na}_{1.5}(\text{Y}_{1.17}\text{Yb}_{0.3}\text{Er}_{0.03})\text{F}_6$ Nanoparticles

Hexagonal $\beta\text{-Na}_{1.5}(\text{Y}_{1.17}\text{Yb}_{0.3}\text{Er}_{0.03})\text{F}_6$ NPs were synthesized by the standard precursor thermolysis method in a high-boiling solvents medium [12,48]. Yttrium, ytterbium, and erbium trifluoroacetates were prepared by dissolving the corresponding rare-earth oxides in a 50 wt.% solution of trifluoroacetic acid and then used as fluoride precursors. For the synthesis of $\beta\text{-Na}_{1.5}(\text{Y}_{1.17}\text{Yb}_{0.3}\text{Er}_{0.03})\text{F}_6$ NPs, 0.78 mmol $(\text{CF}_3\text{COO})_3\text{Y}$, 0.20 mmol $(\text{CF}_3\text{COO})_3\text{Yb}$, 0.02 mmol $(\text{CF}_3\text{COO})_3\text{Er}$, and 1.00 mmol CF_3COONa were added to a 100 mL three-necked flask containing 15 mL of oleic acid and 15 mL of 1-octadecene. The resulting mixture was heated to 600 K with a heating rate of 20 K/min under Ar flow and kept at this temperature for 40 min. After cooling the flask to RT, NPs were collected by centrifugation of the resulting mixture at 6000 rpm for 15 min and washed three times with 2-propanol. The prepared particles were dispersed in 10 mL of hexane and used for further analysis.

2.5. XRD Analysis

XRD patterns of the analyzed samples were carried out on an X-ray powder diffractometer MiniFlex 600 (Rigaku, Tokyo, Japan) with $\text{CuK}\alpha$ radiation. Diffraction peaks were recorded within the angle range 2θ from 10° to 100° . The phases were identified using the ICDD PDF-2 (2014). The unit-cell parameters were calculated by the Le Bail full-profile fitting (the Jana2006 software).

2.6. Electron Microscopy Characterization

TEM, including selected area electron diffraction (SAED), high-angle annular dark-field scanning TEM (HAADF-STEM), and simultaneously acquired energy-dispersive X-ray spectroscopy (EDS) elemental mapping analysis were performed on a Tecnai Osiris (FEI, Hillsboro, OR, USA) electron microscope operated at 200 kV and equipped with a Super-X SDD high-sensitivity EDX spectrometer. TEM samples were prepared by dropping nanoparticle hexane dispersion onto the carbon-coated Cu TEM grids. The experimental images were processed using the Digital Micrograph software 2.31 (Gatan Inc., Pleasanton, CA, USA). Interpretation of the electron diffraction patterns and HRTEM diffractograms were carried out using the Java Electron Microscopy Software (JEMS) [49].

2.7. Fluorescent Spectroscopy Analysis

The photoluminescence characteristics of the produced NPs were performed on a Fluorolog-3 fluorometer (HJY, Longjumeau, France) equipped with the Hamamatsu photomultiplier R929P and H10330A-75 tubes (Hamamatsu Photonics, Shizuoka, Japan) for registration of luminescent radiation in the visible (350–850 nm) and IR (1100–1700 nm) optical ranges, respectively. A semiconductor ATC IR laser $\lambda = 975$ nm (pump power density was 25 W/cm^2) was used as an excitation light source. The luminescence decay curves were recorded on a WaveRunner 9000-MS high-speed oscilloscope (Teledyne LeCroy, Chestnut Ridge, NY, USA) under excitation by a semiconductor ATC IR laser ($\lambda = 975$ nm) in a pulsed mode. The pump power density was 115 and 55 W/cm^2 ; the pulse repetition rate was 200 and 50 Hz for recording the decay curves in the visible and IR optical ranges, respectively. The laser pulse duration was 1000 μs .

3. Results

3.1. Growth and Optical Properties of $\text{Ba}(\text{Y}_{0.964}\text{Yb}_{0.030}\text{Er}_{0.006})_2\text{F}_8$ Crystal

$\text{Ba}(\text{Y}_{0.964}\text{Yb}_{0.030}\text{Er}_{0.006})_2\text{F}_8$ crystals with a diameter of 10 mm and a length of up to 40 mm were successfully grown (Figure 1a). Crystal boules were optically transparent, no light-scattering inclusions and cracks were observed. The crystals demonstrate bright green luminescence under IR excitation (Figure 1b).

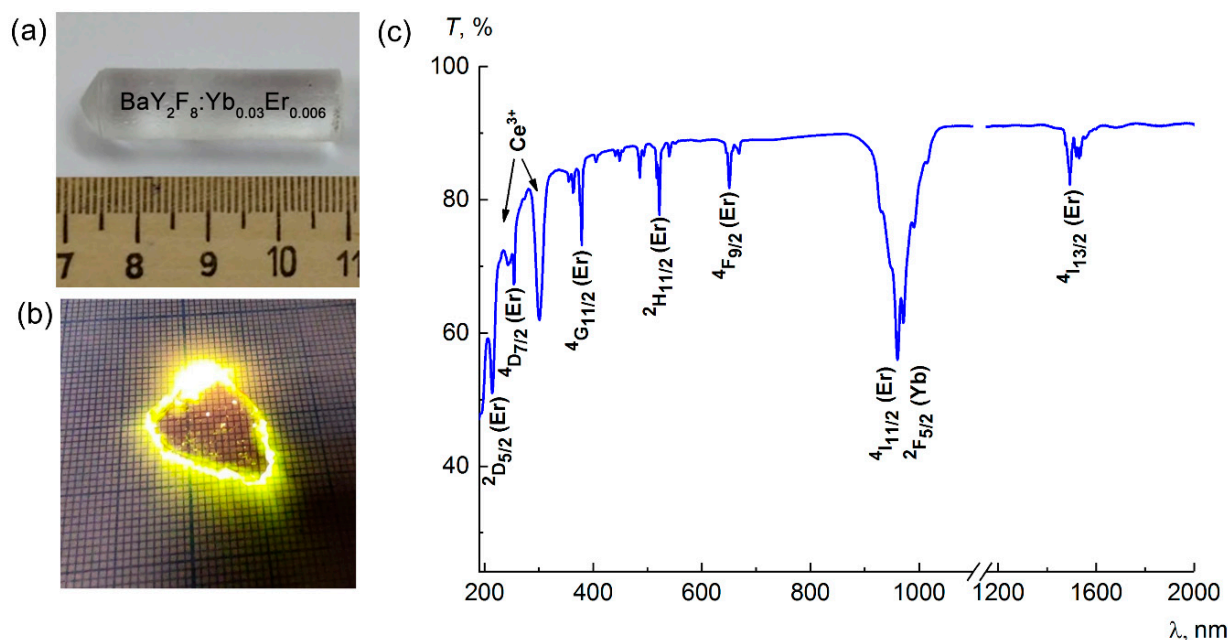


Figure 1. (a) The as-grown crystal appearance, (b) intense green luminescence of the bulk crystal under excitation with $\lambda = 975$ nm radiation, and (c) the transmission spectrum of the $\text{Ba}(\text{Y}_{0.964}\text{Yb}_{0.030}\text{Er}_{0.006})_2\text{F}_8$ crystal, the sample thickness was 2 mm.

In the optical transmission spectrum (Figure 1c), the absorption bands in the UV (380 nm), visible (487, 522, 650 nm), and IR (1480–1530 nm) regions are assigned to electric dipole intra-configurational $4f$ – $4f$ transitions in Er^{3+} ions, while the intense band in the region of 960–980 nm is attributed to the absorption of the Yb^{3+} ions. Weak additional bands registered at 246 and 300 nm are associated with uncontrolled contamination of a Ce^{3+} ions impurity [50].

3.2. XRD Analysis of a Bulk Crystal, $\text{Ba}(\text{Y}_{0.964}\text{Yb}_{0.030}\text{Er}_{0.006})_2\text{F}_8$ and $\beta\text{-Na}_{1.5}(\text{Y}_{1.17}\text{Yb}_{0.3}\text{Er}_{0.03})\text{F}_6$ Nanoparticles

The phase purity and the assignment of grown crystals and fabricated NPs to a monoclinic (sp. gr. C_2/m) BaTm_2F_8 -type structure [51] were confirmed by XRD analysis

(Figure 2). Comparison of the calculated structural characteristics of bulk and milled $\text{Ba}(\text{Y}_{0.964}\text{Yb}_{0.030}\text{Er}_{0.006})_2\text{F}_8$ samples, shown in Table 1, confirms the absence of changes in the crystal structure during the milling process. A minor reducing in the lattice parameters for the nanosized crystal sample is probably attributed to the originating mechanical compression strains during such high energy treatment. A significant broadening and a decrease in the intensity patterns for fabricated NPs indirectly indicate the crystallite sizes reducing and a transition to nanoscale. No impurity phases were observed. The reference $\beta\text{-Na}_{1.5}(\text{Y}_{1.17}\text{Yb}_{0.3}\text{Er}_{0.03})\text{F}_6$ particles synthesized by thermolysis are single-phase and crystallize in a gagarinite $\beta\text{-Na}_{1.5}\text{Y}_{1.5}\text{F}_6$ structure type (sp. gr. $P6_3/m$) [52].

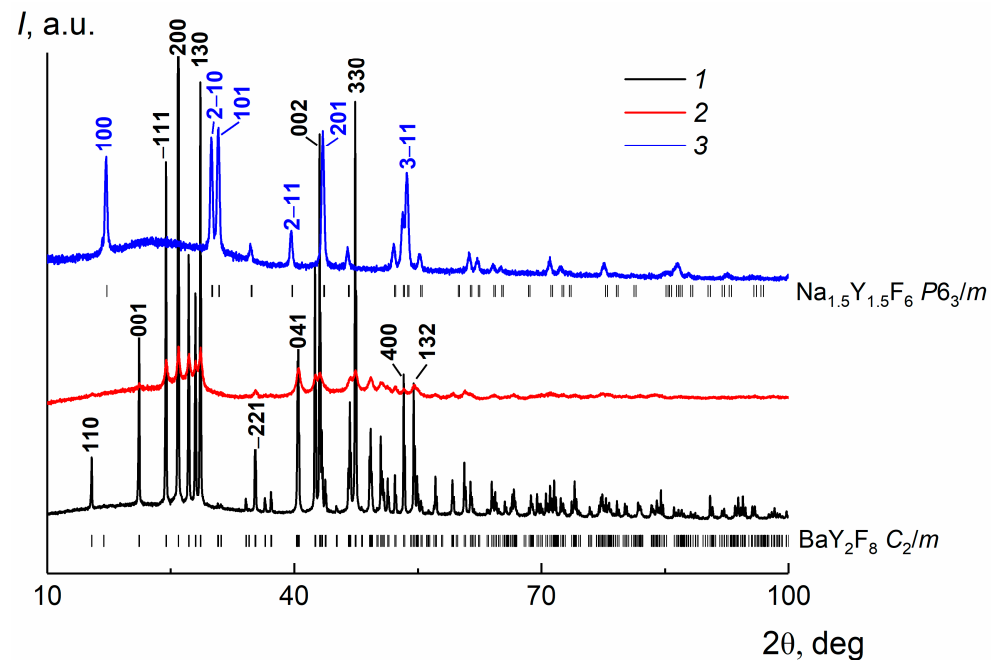


Figure 2. XRD patterns of a bulk $\text{Ba}(\text{Y}_{0.964}\text{Yb}_{0.030}\text{Er}_{0.006})_2\text{F}_8$ crystal (1), $\text{Ba}(\text{Y}_{0.964}\text{Yb}_{0.030}\text{Er}_{0.006})_2\text{F}_8$ particles, produced by milling procedure (2), $\beta\text{-Na}_{1.5}(\text{Y}_{1.17}\text{Yb}_{0.3}\text{Er}_{0.03})\text{F}_6$ NPs, synthesized by thermolysis (3). The positions of the Bragg reflection peaks for the specified space groups are indicated.

Table 1. Calculated unit cell parameters for a bulk $\text{Ba}(\text{Y}_{0.964}\text{Yb}_{0.030}\text{Er}_{0.006})_2\text{F}_8$ crystal and nanodispersed particles and $\beta\text{-Na}_{1.5}(\text{Y}_{1.17}\text{Yb}_{0.3}\text{Er}_{0.03})\text{F}_6$ NPs, synthesized by thermolysis.

	Space Group	Unit Cell Parameters, Å
bulk $\text{Ba}(\text{Y}_{0.964}\text{Yb}_{0.030}\text{Er}_{0.006})_2\text{F}_8$	C_2/m	$a = 6.971(1), b = 10.506(1), c = 4.257(1), \beta = 99.676^\circ$
milled $\text{Ba}(\text{Y}_{0.964}\text{Yb}_{0.030}\text{Er}_{0.006})_2\text{F}_8$	C_2/m	$a = 6.969(3), b = 10.502(1), c = 4.254(1), \beta = 99.676^\circ$
$\beta\text{-Na}_{1.5}(\text{Y}_{1.17}\text{Yb}_{0.3}\text{Er}_{0.03})\text{F}_6$	$P6_3/m$	$a = 5.972(1), c = 3.505(1)$

3.3. TEM Analysis of $\text{Ba}(\text{Y}_{0.964}\text{Yb}_{0.030}\text{Er}_{0.006})_2\text{F}_8$ and $\beta\text{-Na}_{1.5}(\text{Y}_{1.17}\text{Yb}_{0.3}\text{Er}_{0.03})\text{F}_6$ Nanoparticles

TEM data demonstrate that the high energy milling of the initial bulk $\text{Ba}(\text{Y}_{0.964}\text{Yb}_{0.030}\text{Er}_{0.006})_2\text{F}_8$ crystal for 10 h leads to the formation of irregular NPs. The HAADF-STEM image of the agglomerate of NPs without any prominent morphological features in a wide size range from 10 to 70 nm is presented in Figure 3a. The electron diffraction pattern (Figure 3b) taken from an agglomerate corresponds to the structure of the initial bulk monoclinic crystal and confirms the above XRD results. No other phases were found. The EDS analysis results also show no changes in the sample elemental composition during the milling process (Figure 3c).

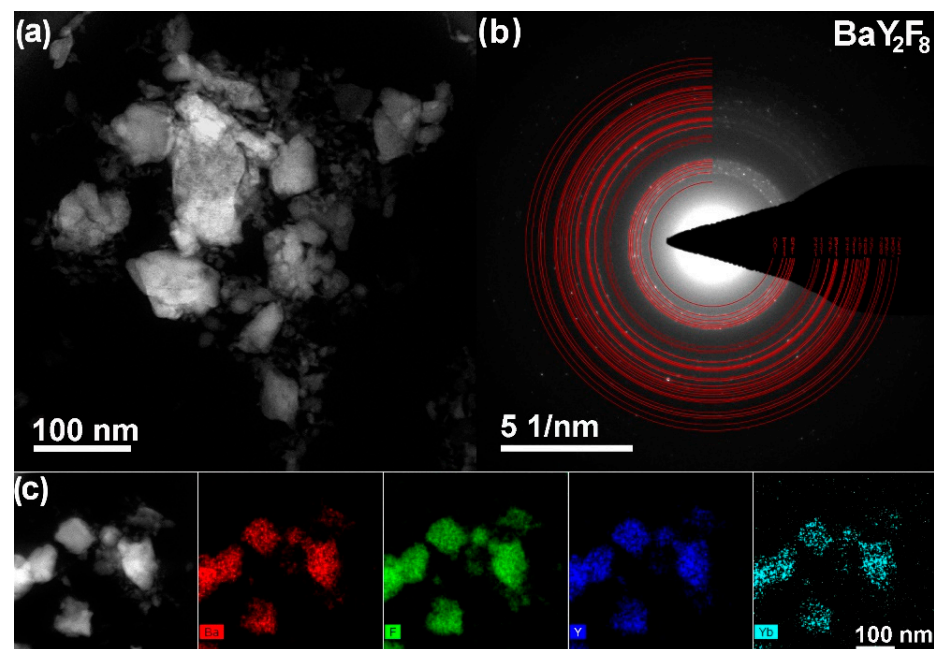


Figure 3. (a) HAADF-STEM image of $\text{Ba}(\text{Y}_{0.964}\text{Yb}_{0.030}\text{Er}_{0.006})_2\text{F}_8$ NPs; (b) the corresponding SAED pattern with the overlaid JEMS simulated rings of the BaY_2F_8 monoclinic phase (sp. gr. C_2/m , $a = 0.698$ nm, $b = 1.051$ nm, $c = 0.4261$ nm, $\beta = 99.676^\circ$); (c) HAADF-STEM image of $\text{Ba}(\text{Y}_{0.964}\text{Yb}_{0.030}\text{Er}_{0.006})_2\text{F}_8$ NPs and the corresponding EDX elemental mapping of Ba L-line (red), F K-line (green), Y L-line (blue), and Yb M-line (light blue).

HRTEM image of the $\text{Ba}(\text{Y}_{0.964}\text{Yb}_{0.030}\text{Er}_{0.006})_2\text{F}_8$ NPs produced by high-energy milling of a bulk crystal and the corresponding diffractograms of nanocrystals A and B are presented in Figure 4. Interpretation of FFT diffractograms using JEMS shows that A and B NPs are oriented along the $[311]$ and $[\bar{3}12]$ directions.

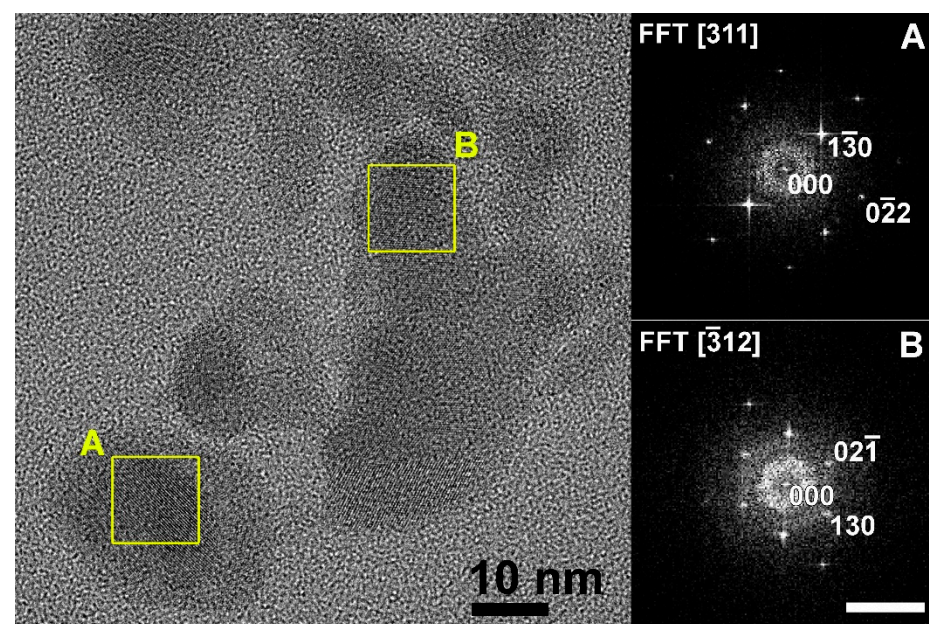


Figure 4. HRTEM image of $\text{Ba}(\text{Y}_{0.964}\text{Yb}_{0.030}\text{Er}_{0.006})_2\text{F}_8$ NPs (A) and (B) their corresponding diffractograms obtained along directions close to $[311]$ and $[\bar{3}12]$; the scale bar on the diffractograms corresponds to 5 nm^{-1} .

TEM image of $\beta\text{-Na}_{1.5}(\text{Y}_{1.17}\text{Yb}_{0.3}\text{Er}_{0.03})\text{F}_6$ nanophosphors is shown in Figure 5. According to TEM data (Figure 5a), the thermolysis method leads to the near-monodisperse $\beta\text{-Na}_{1.5}(\text{Y}_{1.17}\text{Yb}_{0.3}\text{Er}_{0.03})\text{F}_6$ NPs in the size range of 21 ± 5 nm. SAED pattern of $\beta\text{-Na}_{1.5}(\text{Y}_{1.17}\text{Yb}_{0.3}\text{Er}_{0.03})\text{F}_6$ particles, shown in Figure 5c, corresponds to the hexagonal crystal structure of $\beta\text{-Na}_{1.5}\text{Y}_{1.5}\text{F}_6$.

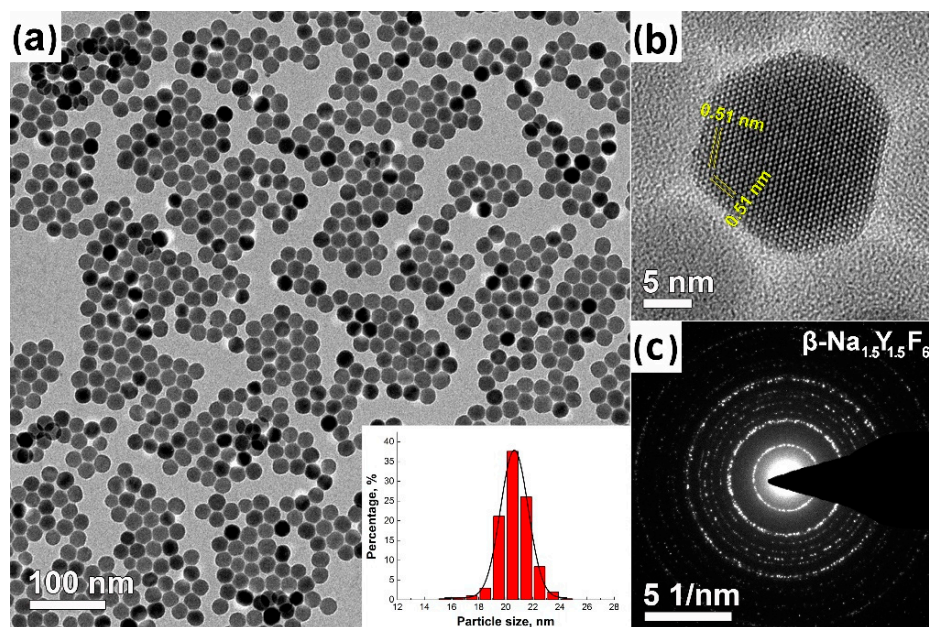


Figure 5. (a) Bright field TEM image with the particle size distribution histogram (insert); (b) HRTEM image of an individual particle close to the [0001] direction; (c) SAED pattern of $\beta\text{-Na}_{1.5}(\text{Y}_{1.17}\text{Yb}_{0.3}\text{Er}_{0.03})\text{F}_6$ NPs, synthesized by thermolysis method.

3.4. Photoluminescence Properties of Bulk and Nanocrystals

Nanosized and bulk $\text{Ba}(\text{Y}_{0.964}\text{Yb}_{0.030}\text{Er}_{0.006})_2\text{F}_8$ samples demonstrate intense visible and IR PL upon excitation by $\lambda = 975$ nm radiation at RT. Intense characteristic luminescence bands, corresponding to $4f\text{-}4f$ energy transitions in Er^{3+} ions, namely transitions from the $^4\text{F}_{7/2}$ (408 nm), $^4\text{H}_{11/2}$ (522 nm), $^4\text{S}_{3/2}$ (540 nm), $^4\text{F}_{9/2}$ (651 nm), and $^4\text{I}_{13/2}$ (1535 nm) multiplet manifolds to the $^4\text{I}_{15/2}$ ground state due to up- and down-conversion energy transfer processes, were observed in the PL spectra (Figure 6a). Comparison the PL spectra of nanosized and bulk $\text{Ba}(\text{Y}_{0.964}\text{Yb}_{0.030}\text{Er}_{0.006})_2\text{F}_8$ samples did not reveal any qualitative differences; no shifts or broadening of the emission bands were detected.

The energy transfer mechanism in BaY_2F_8 crystals co-doped with Yb^{3+} and Er^{3+} ions is shown in Figure 7. Upon absorption of 975 nm photon, Yb^{3+} ions are excited from the $^2\text{F}_{7/2}$ ground state to $^2\text{F}_{5/2}$ state, and then non-radiatively transfer energy to neighboring Er^{3+} ions, populating their intermediate $^4\text{I}_{11/2}$ state. As a result of the successive absorption of two photons, Er^{3+} ions are excited to the $^4\text{F}_{7/2}$ state, which can non-radiatively decay to the $^2\text{H}_{11/2}$, $^4\text{S}_{3/2}$, and $^4\text{F}_{9/2}$ electronic states, followed by radiative green $^4\text{S}_{3/2} \rightarrow ^4\text{I}_{15/2}$ (522 nm), $^2\text{H}_{11/2} \rightarrow ^4\text{I}_{15/2}$ (540 nm), and red $^4\text{F}_{9/2} \rightarrow ^4\text{I}_{15/2}$ (650 nm) characteristic luminescent transitions. Additionally, Er^{3+} ions can be excited to the $^2\text{H}_{9/2}$ state by a three-photon absorption process, followed by a $^2\text{H}_{9/2} \rightarrow ^4\text{I}_{15/2}$ radiative transition at a wavelength $\lambda = 408$ nm. The IR luminescence (1535 nm) results from a radiative decay of the long-lived intermediate $^4\text{I}_{11/2}$ state ($^4\text{H}_{11/2} \rightarrow ^4\text{I}_{15/2}$).

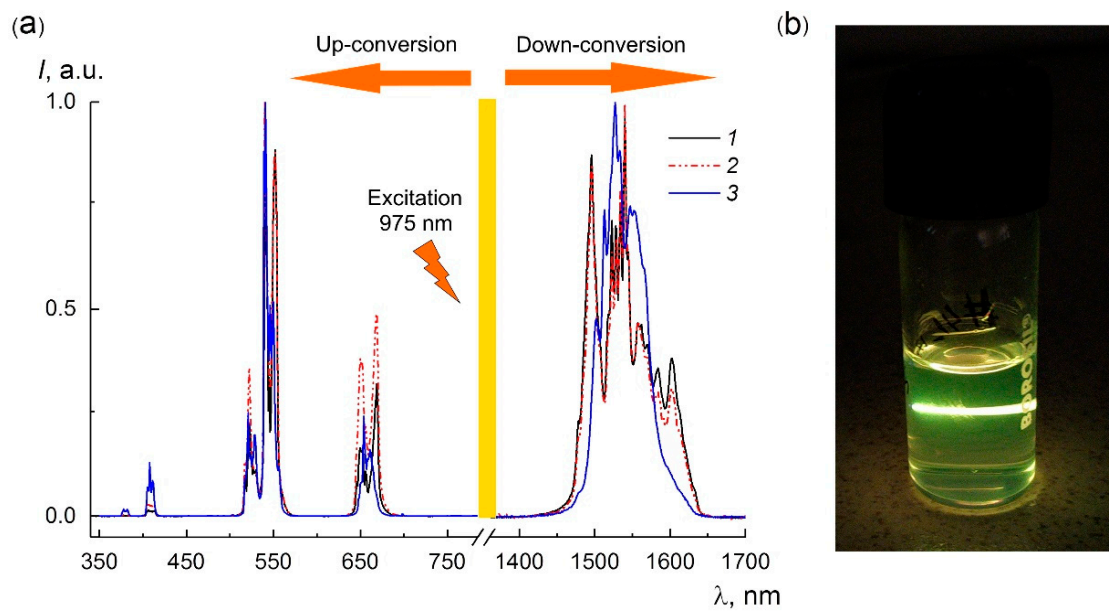


Figure 6. (a) The RT PL spectra of a bulk $\text{Ba}(\text{Y}_{0.964}\text{Yb}_{0.030}\text{Er}_{0.006})_2\text{F}_8$ crystal (1), $\text{Ba}(\text{Y}_{0.964}\text{Yb}_{0.030}\text{Er}_{0.006})_2\text{F}_8$ particles (2), and $\beta\text{-Na}_{1.5}(\text{Y}_{1.17}\text{Yb}_{0.3}\text{Er}_{0.03})\text{F}_6$ (3) NPs upon excitation by $\lambda = 975$ nm radiation; (b) the appearance of a $\text{Ba}(\text{Y}_{0.964}\text{Yb}_{0.030}\text{Er}_{0.006})_2\text{F}_8$ colloid, performing intense green luminescence upon IR excitation ($\lambda = 975$ nm). The luminescence spectra are normalized relative to the wavelength corresponding to the maximum radiation intensity in the visible (540 nm) and IR ranges (1535 nm).

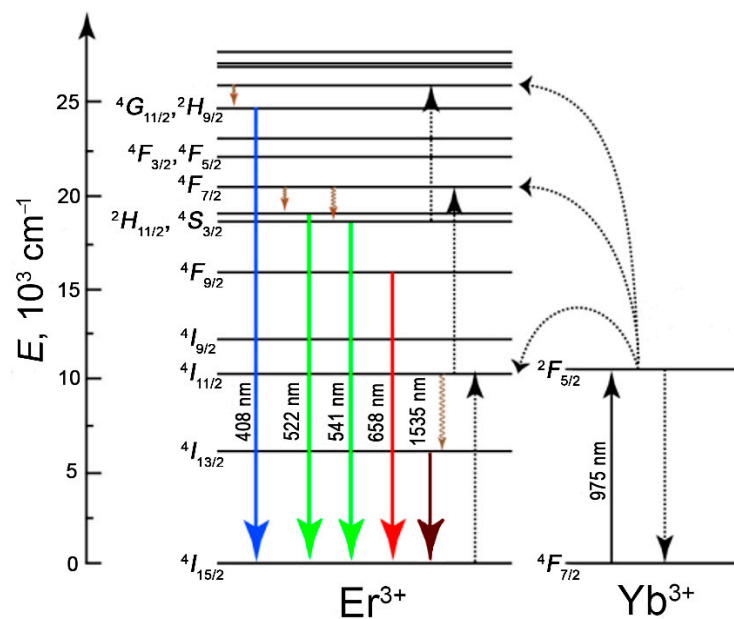


Figure 7. Simplified energy level diagram and possible up- and down-conversion luminescence mechanisms in BaY_2F_8 crystals co-doped with $\text{Yb}^{3+}/\text{Er}^{3+}$ ions.

The PL decay kinetics of the most intense spectral bands at 540, 650, and 1535 nm for $\text{Ba}(\text{Y}_{0.964}\text{Yb}_{0.030}\text{Er}_{0.006})_2\text{F}_8$ samples are shown in Figure 8. Each decay curve is well fitted in a single-exponential dependence:

$$I(t) = I_0 * \exp\left(-\frac{t}{\tau}\right),$$

where $I(t)$ is the PL intensity at time t ; I_0 is the PL intensity at the end of the laser excitation pulse, τ is the average lifetime of the excited state.

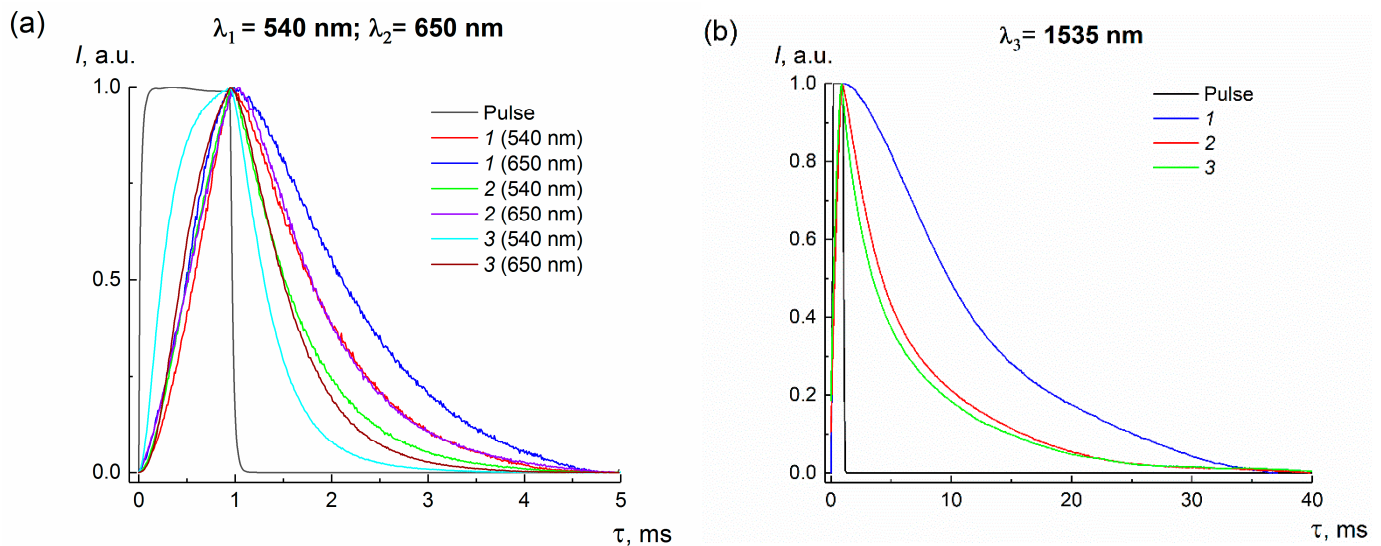


Figure 8. Decay curves of luminescence emission bands in (a) visible and (b) IR spectral ranges of bulk $\text{Ba}(\text{Y}_{0.964}\text{Yb}_{0.030}\text{Er}_{0.006})_2\text{F}_8$ crystal (1), nanodispersed $\text{Ba}(\text{Y}_{0.964}\text{Yb}_{0.030}\text{Er}_{0.006})_2\text{F}_8$ particles (2), $\beta\text{-Na}_{1.5}(\text{Y}_{1.17}\text{Yb}_{0.3}\text{Er}_{0.03})\text{F}_6$ NPs (3) upon IR excitation ($\lambda = 975$ nm).

The calculated PL lifetimes for the studied samples are presented in Table 2. A significant decrease in the lifetime for each PL band is observed for $\text{Ba}(\text{Y}_{0.964}\text{Yb}_{0.030}\text{Er}_{0.006})_2\text{F}_8$ NPs with respect to that for a bulk crystal. This phenomenon is associated with an increase in the surface-to-volume ratio for the nanosized particles. Milling NPs have a high concentration of surface defects generated by strains in the crystallites during the mechanical milling process. The interaction of active Er^{3+} centers, lying on the particle surface, with these defects leads to a significant PL quenching.

Table 2. The PL lifetimes of Er^{3+} excited states in specified compositions.

	τ , ms		
	$\lambda_1 = 540$ nm	$\lambda_2 = 650$ nm	$\lambda_3 = 1535$ nm
bulk $\text{Ba}(\text{Y}_{0.964}\text{Yb}_{0.030}\text{Er}_{0.006})_2\text{F}_8$	0.873	1.200	11.420
milling $\text{Ba}(\text{Y}_{0.964}\text{Yb}_{0.030}\text{Er}_{0.006})_2\text{F}_8$	0.679	0.823	7.530
$\beta\text{-Na}_{1.5}(\text{Y}_{1.17}\text{Yb}_{0.3}\text{Er}_{0.03})\text{F}_6$	0.380	0.527	6.950

A comparative analysis of the PL spectra of $\text{Ba}(\text{Y}_{0.964}\text{Yb}_{0.030}\text{Er}_{0.006})_2\text{F}_8$ and reference $\beta\text{-Na}_{1.5}(\text{Y}_{1.17}\text{Yb}_{0.3}\text{Er}_{0.03})\text{F}_6$ NPs demonstrates the maxima position shifts and the broadening of the spectral lines for a milling sample (Figure 6a). A strong splitting of PL bands for $\text{Ba}(\text{Y}_{0.964}\text{Yb}_{0.030}\text{Er}_{0.006})_2\text{F}_8$ NPs is observed due to a local symmetry lowering of the active centers. The local symmetry of REE ions in the BaY_2F_8 and $\beta\text{-NaYF}_4$ crystal hosts is C_2 and C_{3h} , respectively. Strong Stark splitting of Er^{3+} electronic levels in the more asymmetric crystal field of the monoclinic BaY_2F_8 matrix leads to a stronger degeneracy of existing metastable energy states, which is more clearly observed in the PL spectrum for $\text{Ba}(\text{Y}_{0.964}\text{Yb}_{0.030}\text{Er}_{0.006})_2\text{F}_8$ in the IR range. Such a degeneracy of states leads to an energy gap increasing between closely spaced $4f$ states of Er^{3+} ions and a reduction in the non-radiative relaxation processes probability and, as a consequence, to a rise in the $^4S_{3/2}$, $^4F_{9/2}$, and $^4I_{13/2}$ states' lifetimes. Therefore, the PL lifetimes of Er^{3+} excited states for the BaY_2F_8 matrix are higher than $\beta\text{-Na}_{1.5}(\text{Y}_{1.17}\text{Yb}_{0.3}\text{Er}_{0.03})\text{F}_6$ ones.

4. Conclusions

In this study, $\text{Ba}(\text{Y}_{0.964}\text{Yb}_{0.030}\text{Er}_{0.006})_2\text{F}_8$ NPs in the size range of 30–70 nm were successfully produced by high-energy milling of the Bridgman-grown single crystals. This scalable and versatile method provides a feasible strategy for the mass production of novel fluorescent nanomaterials in a narrow size range that are currently difficult to prepare by available chemical approaches. $\text{Ba}(\text{Y}_{0.964}\text{Yb}_{0.030}\text{Er}_{0.006})_2\text{F}_8$ NPs demonstrate a bright PL in a wide spectral range, which provides great opportunities for applications of these nanophosphors in photonics and biotechnology, for example, as visible and NIR luminescent labels. Further optimization of the milling procedure, namely the adjustment of nanodispersion technological parameters and suitable hydrophobic or hydrophilic surfactants for the nano-sized fraction stabilizing, will provide the possibility to control NP sizes in a narrower range. Optimization of REE doping content and the particle surface passivation by coating a protective shell will significantly enhance the PL properties of studied NPs and are the object of future research.

We believe that BaY_2F_8 -based NPs will occupy a rightful place in nanotechnology, the same as the commonly used $\beta\text{-NaREF}_4$ nanocrystals, which are the most efficient PL nanomaterials to date.

Author Contributions: D.N.K., M.S.S.D. and V.V.K. were involved in the development of the investigation concept; D.N.K. performed crystal growth experiments; A.V.K. performed the synthesis of nanoscale samples; A.V.K. and D.N.K. performed the phase composition analysis of the prepared samples; N.A.A. performed the TEM analysis; A.V.K. and K.V.K. performed the investigation of spectroscopic properties; A.V.K. performed the original draft preparation of the manuscript; N.A.A., K.V.K. and D.N.K. reviewed and edited the draft manuscript; D.N.K. coordinated the scientific group. All authors have read and agreed to the published version of the manuscript.

Funding: This research was funded by the Russian Foundation for Basic Research (project No. 20-52-56017) and Iran National Science Foundation (project No. 99004620) in part concerning the fluoride crystal growth and nanoparticle synthesis and by the Ministry of Science and Higher Education of the Russian Federation within the State assignments of the Federal Scientific Research Centre “Crystallography and Photonics” of the Russian Academy of Sciences in part concerning crystal sample characterization using the equipment of the Shared Research Center.

Informed Consent Statement: Not applicable.

Data Availability Statement: Data sharing not applicable.

Acknowledgments: The authors are deeply grateful to I.V. Krylov and B.V. Nabatov for their help in carrying out the experiments and fruitful discussions.

Conflicts of Interest: The authors declare no conflict of interest. The funders had no role in the design of the study; in the collection, analyses or interpretation of the data; in the writing of the manuscript or in the decision to publish the results.

References

- Meruga, J.M.; Cross, W.M.; May, P.S.; Luu, Q.; Crawford, G.A.; Kellar, J.J. Security printing of covert quick response codes using upconverting nanoparticle inks. *Nanotechnology* **2012**, *23*, 395201. [\[CrossRef\]](#) [\[PubMed\]](#)
- Zhu, X.; Feng, W.; Chang, J.; Tan, Y.-W.; Li, J.; Chen, M.; Sun, Y.; Li, F. Temperature-feedback upconversion nanocomposite for accurate photothermal therapy at facile temperature. *Nat. Commun.* **2016**, *7*, 10437. [\[CrossRef\]](#) [\[PubMed\]](#)
- Generalova, A.; Chichkov, B.; Khaydukov, E. Multicomponent nanocrystals with anti-Stokes luminescence as contrast agents for modern imaging techniques. *Adv. Colloid Interface Sci.* **2017**, *245*, 1–19. [\[CrossRef\]](#) [\[PubMed\]](#)
- Liu, X.; Wang, Y.; Li, X.; Yi, Z.; Deng, R.; Liang, L.; Xie, X.; Loong, D.T.B.; Song, S.; Fan, D.; et al. Binary temporal upconversion codes of Mn^{2+} -activated nanoparticles for multilevel anti-counterfeiting. *Nat. Commun.* **2017**, *8*, 899. [\[CrossRef\]](#) [\[PubMed\]](#)
- Tiwari, S.P.; Maurya, S.K.; Yadav, R.S.; Kumar, A.; Kumar, V.; Joubert, M.-F.; Swart, H.C. Future prospects of fluoride based upconversion nanoparticles for emerging applications in biomedical and energy harvesting. *J. Vac. Sci. Technol. B* **2018**, *36*, 060801. [\[CrossRef\]](#)
- Xu, J.; Gulzar, A.; Yang, P.; Bi, H.; Yang, D.; Gai, S.; He, F.; Lin, J.; Xing, B.; Jin, D. Recent advances in near-infrared emitting lanthanide-doped nanoconstructs: Mechanism, design and application for bioimaging. *Coord. Chem. Rev.* **2018**, *381*, 104–134. [\[CrossRef\]](#)

7. Karimov, D.N.; Demina, P.A.; Koshelev, A.V.; Rocheva, V.V.; Sokovikov, A.V.; Generalova, A.N.; Zubov, V.P.; Khaydukov, E.V.; Koval'Chuk, M.V.; Panchenko, V.Y. Upconversion Nanoparticles: Synthesis, Photoluminescence Properties, and Applications. *Nanotechnol. Russ.* **2020**, *15*, 655–678. [\[CrossRef\]](#)
8. Nadort, A.; Zhao, J.; Goldys, E.M. Lanthanide upconversion luminescence at the nanoscale: Fundamentals and optical properties. *Nanoscale* **2016**, *8*, 13099–13130. [\[CrossRef\]](#)
9. Du, Y.-P.; Sun, X.; Zhang, Y.-W.; Yan, Z.-G.; Sun, L.-D.; Yan, C.-H. Uniform Alkaline Earth Fluoride Nanocrystals with Diverse Shapes Grown from Thermolysis of Metal Trifluoroacetates in Hot Surfactant Solutions. *Cryst. Growth Des.* **2009**, *9*, 2013–2019. [\[CrossRef\]](#)
10. Fedorov, P.P.; Luginina, A.A.; Kuznetsov, S.; Osiko, V.V. Nanofluorides. *J. Fluor. Chem.* **2011**, *132*, 1012–1039. [\[CrossRef\]](#)
11. Cheng, T.; Marin, R.; Skripka, A.; Vetrone, F. Small and Bright Lithium-Based Upconverting Nanoparticles. *J. Am. Chem. Soc.* **2018**, *140*, 12890–12899. [\[CrossRef\]](#) [\[PubMed\]](#)
12. Mai, H.-X.; Zhang, Y.-W.; Si, R.; Yan, Z.-G.; Sun, L.-D.; You, L.-P.; Yan, C.-H. High-Quality Sodium Rare-Earth Fluoride Nanocrystals: Controlled Synthesis and Optical Properties. *J. Am. Chem. Soc.* **2006**, *128*, 6426–6436. [\[CrossRef\]](#) [\[PubMed\]](#)
13. You, W.; Tu, D.; Zheng, W.; Shang, X.; Song, X.; Zhou, S.; Liu, Y.; Li, R.; Chen, X. Large-scale synthesis of uniform lanthanide-doped NaREF₄ upconversion/downshifting nanoprobe for bioapplications. *Nanoscale* **2018**, *10*, 11477–11484. [\[CrossRef\]](#) [\[PubMed\]](#)
14. Grzyb, T.; Balabhadra, S.; Przybylska, D.; Węclawiak, M. Upconversion luminescence in BaYF₅, BaGdF₅ and BaLuF₅ nanocrystals doped with Yb³⁺/Ho³⁺, Yb³⁺/Er³⁺ or Yb³⁺/Tm³⁺ ions. *J. Alloys Compd.* **2015**, *649*, 606–616. [\[CrossRef\]](#)
15. Li, C.; Xu, Z.; Yang, D.; Cheng, Z.; Hou, Z.; Ma, P.; Lian, H.; Lin, J. Well-dispersed KRE₃F₁₀ (RE = Sm–Lu, Y) nanocrystals: Solvothermal synthesis and luminescence properties. *CrystEngComm* **2011**, *14*, 670–678. [\[CrossRef\]](#)
16. Razumkova, I.A.; Denisenko, Y.G.; Boyko, A.N.; Ikonnikov, D.A.; Aleksandrovsky, A.S.; Azarapin, N.O.; Andreev, O.V. Synthesis and Upconversion Luminescence in LaF₃:Yb³⁺, Ho³⁺, GdF₃:Yb³⁺, Tm³⁺ and YF₃:Yb³⁺, Er³⁺ obtained from Sulfide Precursors. *Z. Anorg. Allg. Chem.* **2019**, *645*, 1393–1401. [\[CrossRef\]](#)
17. Boyer, J.-C.; Cuccia, A.L.A.; Capobianco, J.A. Synthesis of Colloidal Upconverting NaYF₄: Er³⁺/Yb³⁺ and Tm³⁺/Yb³⁺ Monodisperse Nanocrystals. *Nano Lett.* **2007**, *7*, 847–852. [\[CrossRef\]](#)
18. Gemini, L.; Schmitz, T.; Kling, R.; Barcikowski, S.; Gökce, B. Upconversion Nanoparticles Synthesized by Ultrashort Pulsed Laser Ablation in Liquid: Effect of the Stabilizing Environment. *ChemPhysChem* **2017**, *18*, 1210–1216. [\[CrossRef\]](#)
19. Sajti, L.; Karimov, D.N.; Rocheva, V.V.; Arkharova, N.A.; Khaydukov, K.V.; Lebedev, O.I.; Voloshin, A.E.; Generalova, A.N.; Chichkov, B.N.; Khaydukov, E.V. Pulsed laser reshaping and fragmentation of upconversion nanoparticles—from hexagonal prisms to 1D nanorods through “Medusa”-like structures. *Nano Res.* **2020**, *14*, 1141–1148. [\[CrossRef\]](#)
20. Yuan, D.; Yi, G.S.; Chow, G.M. Effects of size and surface on luminescence properties of submicron upconversion NaYF₄: Yb, Er particles. *J. Mater. Res.* **2009**, *24*, 2042–2050. [\[CrossRef\]](#)
21. Patel, D.N.; Sarkisov, S.S.; Darwish, A.M.; Ballato, J. Optical gain in capillary light guides filled with NaYF₄: Yb³⁺, Er³⁺ nanocolloids. *Opt. Express* **2016**, *24*, 21147–21158. [\[CrossRef\]](#) [\[PubMed\]](#)
22. Sobolev, B.; Tkachenko, N. Phase diagrams of BaF₂-(Y, Ln)F₃ systems. *J. Less Common Met.* **1982**, *85*, 155–170. [\[CrossRef\]](#)
23. Maksimov, B.A.; Solans, K.; Dudka, A.P.; Genkina, E.A.; Font-Badria, M.; Buchinskaya, I.I.; Loshmanov, A.A.; Golubev, A.M.; Simonov, V.I.; Font-Altaba, M.; et al. The fluorite-matrix-based Ba₄R₃F₁₇ (R = Y, Yb) crystal structure. Ordering of cations and specific features of the anionic motif. *Crystallogr. Rep.* **1996**, *41*, 56–64.
24. Greis, O.; Stede, P.; Kieser, M. Darstellung und Eigenschaften der Ternären Verbindungen BaSe₂F₈ mit SE = Dy—Lu und Y. *Z. Anorg. Allg. Chem.* **1981**, *477*, 133–138. [\[CrossRef\]](#)
25. Guggenheim, H.J.; Johnson, L.F. New fluoride compounds for efficient infrared-to-visible conversion. *Appl. Phys. Lett.* **1969**, *15*, 51–52. [\[CrossRef\]](#)
26. Johnson, L.F.; Guggenheim, H.J. Infrared-Pumped Visible Laser. *Appl. Phys. Lett.* **1971**, *19*, 44–47. [\[CrossRef\]](#)
27. Pollack, S.A.; Chang, D.B.; McFarlane, R.A.; Jenssen, H. Infrared (Er)BaY₂F₈ laser pumped through di- and tri-ionic upconversion processes. *J. Appl. Phys.* **1990**, *67*, 648–653. [\[CrossRef\]](#)
28. Kaminskii, A.A.; Kochubei, S.A.; Naumochkin, K.N.; Pestryakov, E.V.; Trunov, V.I.; Uvarova, T.V. Amplification of ultraviolet radiation due to the 5d–4f interconfigurational transition of the Ce³⁺ ion in BaY₂F₈. *Sov. J. Quantum Electron.* **1989**, *19*, 340–342. [\[CrossRef\]](#)
29. Noginov, M.A.; Curley, M.; Venkateswarlu, P.; Williams, A.; Jenssen, H.P. Excitation scheme for the upper energy levels in a Tm:Yb:BaY₂F₈ laser crystal. *J. Opt. Soc. Am. B* **1997**, *14*, 2126–2136. [\[CrossRef\]](#)
30. Uvarova, T.V.; Pushkar, A.A.; Uvarova, A.G. Multi-bands active media on the basis of BaY₂F₈ single crystals for up-conversion solid-state lasers with diode pumping. *Phys. Status Solidi C* **2011**, *8*, 2911–2914. [\[CrossRef\]](#)
31. Spijker, J.V.; Dorenbos, P.; van Eijk, C.; Jacobs, J.; Hartog, H.D.; Korolev, N. Luminescence and scintillation properties of BaY₂F₈:Ce³⁺, BaLu₂F₈ and BaLu₂F₈:Ce³⁺. *J. Lumin.* **1999**, *85*, 11–19. [\[CrossRef\]](#)
32. de Mello, A.C.; Andrade, A.B.; Nakamura, G.H.; Baldochi, S.L.; Valerio, M.E. Scintillation mechanism of Tb³⁺ doped BaY₂F₈. *Opt. Mater.* **2010**, *32*, 1337–1340. [\[CrossRef\]](#)
33. Kurosawa, S.; Yanagida, T.; Pejchal, J.; Fukuda, K.; Kawaguchi, N.; Ishizu, S.; Suyama, T.; Nakagawa, M.; Yokota, Y.; Nikl, M.; et al. Evaluation of Nd:BaY₂F₈ for VUV scintillator. *Radiat. Meas.* **2013**, *55*, 108–111. [\[CrossRef\]](#)

34. Liu, H.; Lu, W.; Wang, H.; Rao, L.; Yi, Z.; Zeng, S.; Hao, J. Simultaneous synthesis and amine-functionalization of single-phase BaYF₅:Yb/Er nanoprobe for dual-modal in vivo upconversion fluorescence and long-lasting X-ray computed tomography imaging. *Nanoscale* **2013**, *5*, 6023–6029. [CrossRef] [PubMed]
35. Nampi, P.P.; Vakurov, A.; Viswambharan, H.; Schneider, J.E.; Drummond-Brydson, R.; Millner, P.A.; Saha, S.; Jose, G. Barium yttrium fluoride based upconversion nanoparticles as dual mode image contrast agents. *Mater. Sci. Eng. C* **2021**, *124*, 111937. [CrossRef] [PubMed]
36. Zhang, C.; Ma, P.A.; Li, C.; Li, G.; Huang, S.; Yang, D.; Shang, M.; Kang, X.; Lin, J. Controllable and white upconversion luminescence in BaYF₅:Ln³⁺ (Ln = Yb, Er, Tm) nanocrystals. *J. Mater. Chem.* **2010**, *21*, 717–723. [CrossRef]
37. Cao, Z.; Zhou, S.; Jiang, G.; Chen, Y.; Duan, C.; Yin, M. Temperature dependent luminescence of Dy³⁺ doped BaYF₅ nanoparticles for optical thermometry. *Curr. Appl. Phys.* **2014**, *14*, 1067–1071. [CrossRef]
38. Haritha, P.; Martin, I.R.; Viswanath, C.D.; Vijaya, N.; Krishnaiah, K.V.; Jayasankar, C.; Haranath, D.; Lavín, V.; Venkatramu, V. Structure, morphology and optical characterization of Dy³⁺-doped BaYF₅ nanocrystals for warm white light emitting devices. *Opt. Mater.* **2017**, *70*, 16–24. [CrossRef]
39. Fedorov, P.P.; Mayakova, M.N.; Kuznetsov, S.V.; Voronov, V.V.; Ermakov, R.P.; Samarina, K.S.; Popov, A.I.; Osiko, V.V. Co-precipitation of yttrium and barium fluorides from aqueous solutions. *Mater. Res. Bull.* **2012**, *47*, 1794–1799. [CrossRef]
40. Karbowiak, M.; Cichos, J. Does BaYF₅ nanocrystals exist?—The BaF₂-YF₃ solid solution revisited using photoluminescence spectroscopy. *J. Alloys Compd.* **2016**, *673*, 258–264. [CrossRef]
41. Grube, J.; Kieke, G. How activator ion concentration affects spectroscopic properties on Ba₄Y₃F₁₇: Er³⁺, Yb³⁺, a new perspective up-conversion material. *J. Lumin.* **2018**, *203*, 376–384. [CrossRef]
42. Pudovkin, M.; Kuznetsov, S.; Proydakova, V.Y.; Voronov, V.; Semashko, V. Luminescent thermometry based on Ba₄Y₃F₁₇:Pr³⁺ and Ba₄Y₃F₁₇:Pr³⁺, Yb³⁺ nanoparticles. *Ceram. Int.* **2020**, *46*, 11658–11666. [CrossRef]
43. Wang, G.; Peng, Q.; Li, Y. Synthesis and upconversion luminescence of BaY₂F₈:Yb³⁺/Er³⁺ nanobelts. *Chem. Commun.* **2010**, *46*, 7528–7529. [CrossRef] [PubMed]
44. Wang, X.; Hou, Y.; Qu, J.; Ding, J.; Lin, H.; Liu, L.; Zhou, Y.; Zeng, F.; Li, C.; Su, Z. Up-conversion photoluminescence properties and energy transfer process of Ho³⁺, Yb³⁺ Co-doped BaY₂F₈ fine fibers. *J. Lumin.* **2019**, *212*, 154–159. [CrossRef]
45. Nair, G.B.; Kumar, A.; Swart, H.; Dhoble, S. Facile precipitation synthesis of green-emitting BaY₂F₈:Yb³⁺, Ho³⁺ upconverting phosphor. *Ceram. Int.* **2019**, *45*, 14205–14213. [CrossRef]
46. Toncelli, A.; Ahmadi, B.; Marchetti, F. Upconversion enhancement in Yb³⁺, Tm³⁺:BaY₂F₈ quasi-nanoparticles. *J. Lumin.* **2012**, *132*, 2268–2274. [CrossRef]
47. Hakim, R.; Damak, K.; Gemmi, M.; Luin, S.; Maalej, R.; Toncelli, A. Pr³⁺:BaY₂F₈ Crystal Nanoparticles (24 nm) Produced by High-Energy Ball Milling: Spectroscopic Characterization and Comparison with Bulk Properties. *J. Phys. Chem. C* **2015**, *119*, 2844–2851. [CrossRef]
48. Boyer, J.-C.; Vetrone, F.; Cuccia, L.A.; Capobianco, J.A. Synthesis of Colloidal Upconverting NaYF₄ Nanocrystals Doped with Er³⁺, Yb³⁺ and Tm³⁺, Yb³⁺ via Thermal Decomposition of Lanthanide Trifluoroacetate Precursors. *J. Am. Chem. Soc.* **2006**, *128*, 7444–7445. [CrossRef]
49. JEMS. Available online: <http://www.jems-saas.ch> (accessed on 15 March 2020).
50. Sani, E.; Toncelli, A.; Tonelli, M. Effect of Cerium codoping on Er:BaY₂F₈ crystals. *Opt. Express* **2005**, *13*, 8980–8992. [CrossRef]
51. Izotova, O.E.; Aleksandrov, V.B. The Crystal Structure of BaTm₂F₈. *Sov. Phys. Dokl.* **1970**, *15*, 525–527.
52. Krämer, K.W.; Biner, D.; Frei, G.; Güdel, H.U.; Hehlen, M.P.; Lüthi, S.R. Hexagonal Sodium Yttrium Fluoride Based Green and Blue Emitting Upconversion Phosphors. *Chem. Mater.* **2004**, *16*, 1244–1251. [CrossRef]